Extracting Urban Parameters of the City of Oldenburg from Hyperspectral, Thermal, and Airborne Laser Scanning Data

Lutz Bannehr, Andreas Schmidt, Dessau-Roßlau, Johannes Piechel & Thomas Luhmann, Oldenburg

Summary: This paper shows how to use different remote sensing sensors and methods to obtain parameters about the urban built-up areas. Within the cooperative research project HiReSens a hyperspectral scanner, an airborne laser scanner, a thermal camera, and a RGB-camera were employed on a small aircraft to determine roof material and geometric parameters as well as heat bridges within the city of Oldenburg, Lower Saxony, Germany.

HiReSens aims to combine various geometrical highly resolved data (50 cm) in order to survey the state of the roof areas. Thermal data were used to obtain the temperature distribution of single roof tops. The hyperspectral data provide information on the roofing materials. Support vector machines (SVM) were used to classify these roof materials. Five out of six roofing materials were clearly detected.

From airborne laser scanning (ALS) data a digital surface model and a digital terrain model were calculated. These models in combination with hyperspectral data form the basis to locate the buildings with the best orientations for solar panels. A decision tree algorithm gives satisfactory results in this case.

The combination of the different datasets offers the opportunity to use synergies between different sensor systems. The central goals were the development of tools for the detection of thermal bridges by means of thermal data, spectral differentiation of roof parameters on the basis of hyperspectral data as well as 3D-capture of buildings from ALS data.

Zusammenfassung: *Ableitung von städtischen Parametern der Stadt Oldenburg durch Hyperspektral-, Thermal- und Airborne Laser Scanning Daten.* Im Rahmen des kooperativen Forschungsprojektes HiReSens, gefördert vom BMBF, wird ein Hyperspektralscanner, ein Airborne Laser Scanner, eine Thermalkamera und eine RGB-Kamera auf einem kleinem Flugzeug, einer Cessna 207, eingesetzt, woraus Parameter der städtischen Bebauung, wie Dachmaterial- und Geometrieparameter sowie Temperaturverteilungen von Dächern, abgeleitet werden.

HiReSens zielt darauf ab, verschiedene geometrisch hochauflösende (50 cm) Daten der Stadt Oldenburg in Niedersachsen zu kombinieren, um Synergien zwischen den unterschiedlich arbeitenden Sensorsystemen zu nutzen. Aus dem digitalen Geländemodell in Kombination mit den Hyperspektraldaten wird eine Dachmaske mittels Entscheidungsbaum-Klassifikation generiert. Aus den Thermaldaten lässt sich die Temperaturverteilung innerhalb einzelner Hausdächer bestimmen, welche Indizien auf mögliche Wärmebrücken geben. Die Hyperspektraldaten liefern spektrale Informationen über Dachmaterialien. Sie werden mit Hilfe eines Support Vector Machine (SVM) Klassifizierungsalgorithmus ermittelt. Fünf von sechs Dachmaterialien sind klar differenzierbar.

Die digitalen Höhenmodelle, abgeleitet aus Airborne Laser Scanner Daten, dienen in Kombination mit den Hyperspektraldaten der Ermittlung von Dächern, die eine optimale Ausrichtung für die Installation von Solaranlagen aufweisen.

Die zentralen Ziele des Projektes sind die Entwicklung von Werkzeugen zum Erkennen von Temperaturverteilungen, spektrale Unterscheidung verschiedener Dachparameter auf Basis der Hyperspektraldaten sowie die 3D-Erfassung von Gebäuden aus den Airborne Laser Scanner Daten.

1 Introduction

Urban development plays an important role in modern times. Questions related to the limited availability of natural resources and energy consumption develop in all parts of the world. The steady progress of urban sealing has influence on the local climate and hence on our well-being. Remote sensing techniques may assist in obtaining the information required to support decision-making processes to sustain or even improve the quality of our environment. In order to address these issues from a planning point of view, 3D data having a high spatial and spectral resolution are very helpful. Airborne data are mostly suitable for these purposes as a trade-off between expansion of the area and acquisition of small details. Especially when using more than one sensor in a flight, airborne methods become fairly cost efficient and can cover larger areas compared to on-site inspections.

Hyperspectral data can be used to differentiate various urban surface cover types (HELDEN et al. 2010, YANG 2011). Due to the strong heterogeneity of urban areas, data of a high geometrical resolution are required. For many applications a resolution (ground sampling distance, GSD) of 50 cm or better is desirable. At a coarser resolution (GSD > 1 m), mixed pixels do no longer allow to separate small details. ROESSNER et al. (2001) used a spectral unmixing algorithm to reduce the problem with DAIS hyperspectral data having a GSD of 7 m, leading to improved classification results compared to standard procedures.

MORI et al. (2008) classified and analysed roof materials in Japan based on a handheld spectrometer using the reflectance between 350 nm – 2,500 nm as a basis. However, only single spots can be handled by this method. BÄHR et al. (2005) and LEMP & WEIDNER (2004) developed an automatic procedure to determine roof parameters from hyperspectral and airborne laser scanner (ALS) data based on segmentation. They distinguish five roof classes. For the classification a partly object-oriented approach was implemented. The classification was based solely on hyperspectral data. New aspects of segmentation and classification were implemented by LEMP & WEIDNER (2005). Additionally, they used slope information to improve the results of roof classification. BRAUN et al. (2012) implemented a method for the fusion of hyperspectral and ALS data to improve SVM classification by kernel composition, modifying the one-against-one cascade and taking into account human knowledge on roof geometries.

Building detection and reconstruction have been important topics of photogrammetric research for many years. For instance, KOKKAS & DOWMAN (2006) introduced a semiautomatic technique for building reconstruction by fusing aerial digital imagery and ALS data. RENTSCH & KRZYSTEK (2009) used ALS data for a 3D reconstruction of roof ridge lines and roof planes. ROTTENSTEINER et al. (2012) compare and evaluate different methods of building detection and 3D reconstruction from airborne image and laserscanning data. KLÄRLE (2009) used ALS data to infer the optimal locations for photo-voltaic solar panels. HILLING & DE LANGE (2010) show a web-based application for deriving the solar potential from ALS data.

For the project HiReSens hyperspectral data in the visible to near infrared spectral range were collected to derive roof parameters of the city of Oldenburg. The hyperspectral data have a spatial resolution of 0.5 m. In addition, thermal and ALS data are gathered to address energy-related issues. Furthermore, aerial images (RGB) are used to enable a precise georeferencing and fusion of all data.

Merging of all these different kinds of data results in a vast pool from which useful information can be extracted. Generally one can say that the accuracy of classification results increases considerably by synergy effects since certain classes can be separated more accurately using additional information unless the features are strongly correlated. For the classification a decision tree (QUINLAN 1986) and the support vector machine (SVM, STEINWART & CHRISTMANN 2008) algorithm are used. The innovative core of this project is the challenging data acquisition:
- high spectral and spatial resolution data,
- a georeferencing accuracy of a few decimetres,
- the fusion of these different data.

The products may serve as additional input data for 3D city models as well as GIS databases.

This paper presents a setup of four different airborne sensors for high spatial resolution remote sensing over urban areas. The data processing is discussed as well as the challenges of combining these high resolution data. From this pool of information some derived products are shown: roof temperature variation, solar potential, and roof material classification.

Two different classification algorithms are applied to derive parameters related to the buildings in a scene. SVM are used to classify up to six different roof materials, whereas a decision tree helps to derive the roof alignment in order to assess the potential of solar energy.

In our study, hyperspectral data are combined with ALS data. In this way we do not only identify roof surfaces which are theoretically suitable for solar power generation, but we identify the surfaces that are really usable for that purpose. These surfaces are often smaller due to tree overhangs. The temperature distribution of roof surfaces which can be an indicator of heat bridges is also visualised.

2 Observations

Different weather conditions are required for data acquisition using airborne hyperspectral, thermal and ALS sensors. For hyperspectral and RGB data acquisition, clear skies and a high sun elevation are desirable. For collecting thermal data the most suitable weather conditions are encountered at night, or in the morning when temperatures are low, without snow or dew, and under a uniform cloud cover. An ALS can be operated under most weather conditions apart from rain, snow, or fog. Also dew prevents a successful data acquisition.

Considering these constraints three flights at different times were performed over the city of Oldenburg, Germany. The total project area size was 3.8 km × 1.8 km. Within this area the work was focused on a core test site of 1.8 km × 1.0 km which hosted the broadest diversity of urban features.

More than 60 GBytes of hyperspectral, thermal and ALS raw data were collected. They were captured using the Cessna 207 aircraft of Milan Geoservice. A system descrip-tion is given in detail by BANNEHR et al. (2006). The RGB images were taken by Alpha Luftbild using an Aquila A210.

2.1 Hyperspectral Observations

The imaging spectrometer AISA+ is a non-cooled system. It serves for monitoring and detection of environmental damage, determination of water constituents of lakes and rivers, forest state examination, and atmospheric research. Up to 244 spectral channels with a bandwidth of 2.5 nm in wavelength can be defined within the spectral range from 400 nm to 980 nm. For the project HiReSens 107 spectral channels with a bandwidth of about 5 nm are used as a trade-off between noise, exposure time and channel bandwidth.

The AISA+ system was radiometrically calibrated by the manufacturer Specim, Finland. According to Specim the calibration accuracy over the spectral range of the imaging spectrometer is about 10 %. This accuracy is not critical for the current investigation because the airborne reference spectra are compared with ground truth spectra. Eleven strips were flown on 16 June 2010 to cover the whole project area. The altitude of 600 m resulted in a GSD of 50 cm.

2.2 IR Measurements

The infrared camera, a FLIR SC3000, enables the detection of small differences in temperature. Thus, it is most suitable to detect thermal bridges and energy losses of buildings by looking at temperature variations within house roofs. The infrared camera has a detector size of 320 × 240 pixels. Its spectral response is between 8 µm and 9 µm. Up to 50 images per second can be taken. For the present project the data acquisition rate was set to 10 Hz. This high sampling rate assures a high overlap in the flight direction and hence minimizes the angular effect of emissivity. During the measurement the standard temperature range of the IR camera was set to the range from –20 °C to 80 °C. This temperature range is resolved with 14 bit, which results in a temperature resolution of 30 mK.

The observations were carried out just before sunrise at an altitude of approximately 500 m on 28 April 2010 (GSD: 55 cm). Fifteen flight strips were needed to cover the total project area, nine of which cover the core test site.

The thermal camera was calibrated geometrically in the laboratory with a 3D test field (Luhmann et al. 2011).

2.3 Airborne Laser Scanning

For the second research flight the Riegl LMS Q560 laser scanner and the thermal camera FLIR SC3000 were on the same aircraft. The resulting ALS point density was about 23 points/m^2. These data were rasterized at a spatial resolution of 25 cm.

2.4 RGB Observations

Alpha Luftbild provided the RGB camera Rollei AIC P45 with 39 megapixels and performed the measurement flight on 25 March 2010. Due to their high spatial resolution, the RGB data are used as a reference for the co-registration of the other sensors, in particular for the hyperspectral and the thermal data. Furthermore, the RGB data served as reference information for defining the training areas in the SVM-based classification. The flight altitude of 580 m resulted in a GSD of about 8.5 cm. The forward and side laps were 68 % and 80 %, respectively.

3   Pre-processing

The AISA+ hyperspectral system and the Riegl airborne laser scanner LMS-Q560 were connected to an IGI CCNS4 and an AEROcontrol GNSS/INS. This system samples the aircraft motion data (roll, pitch, yaw) with 256 Hz and the GNSS data with 10 Hz. The GNSS data is post processed using SAPOS correction data. For the ALS data an accuracy of 0.2 m is achieved both in planimetry and height. After the geometrical co-registration, which will be explained in the subsequent sections, all data were transformed into UTM 32N, WGS 84.

3.1 Rollei AIC-P45

The 56 images of the core region were oriented using 18 manhole covers as ground control points (GCPs). The GCPs were collected using DGPS. More than 700 tie points were used. Two to three points were picked manually for each image. The rest were picked automatically. A digital surface model (DSM) derived from the ALS data (section 3.4) was used to generate an orthophoto mosaic of the whole project area (GSD: 10 cm). This mosaic, which contained double mappings, was used for precise georeferencing of the hyperspectral data. We also generated a DSM of the core area by semi-global matching (Hirschmüller 2008) from the RGB images. The software also delivers a true orthophoto (GSD: 8.5 cm), which we used to generate the reference for the SVM-based classification (section 4.4).

3.2 FLIR SC3000

The surface temperature range during the field experiment was between 3.5 °C and 9.5 °C. This agrees with in-situ measurements of the collected temperature data. The thermal camera was not connected to a GNSS/INS. Therefore, the data were georeferenced by aerotriangulation using ground control and tie points. Because of the very high image overlap, only every fourth image was used. The result is a thermal image mosaic based on the ALS data with a GSD of 50 cm (Fig. 1). Buildings are generally cooler (dark purple) than the surrounding roads and non-built-up areas. The white areas correspond to water. One also can see temperature variations both between and within individual buildings. For a more in-depth analysis it is necessary to extract the thermal features in detail.

The interpretation of thermal images must be done carefully because the measured temperatures depend on the emissivity ε of the roof materials, which are different in general. Variations of ε between 0.80–0.94 and more are very common. This can result in a temperature difference of several Kelvin, depending on the temperature level itself. Without any further information about a building, it is not possible to decide whether the temperature
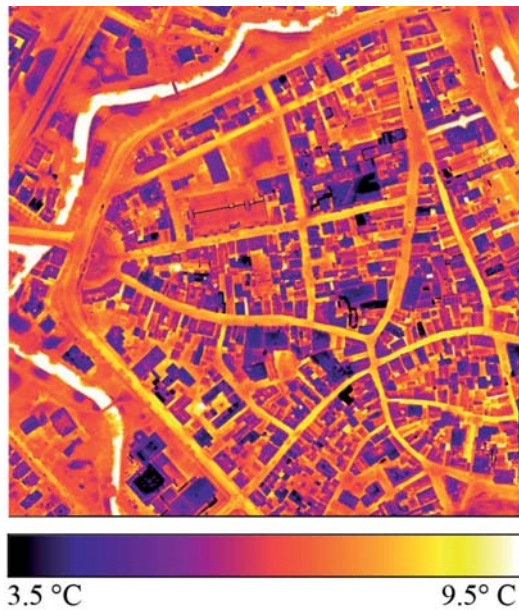
Fig. 1: A 500 m × 500 m subset of the thermal infrared orthorectified image section of Oldenburg (GSD: 50 cm).

distribution is due to the variation of the emissivity or arises from different surface temperatures. In section 4.1, a method to highlight the temperature distribution within the individual buildings is presented.

The spectral band used by the infrared camera (8 µm–9 µm) is within an atmospheric window (8 µm–14 µm). The influence of the atmosphere on the signal is expected to be rather low. Nevertheless, radiative transfer calculations using MODTRAN (BERK et al. 2006) were carried out for a flight altitude of 500 m assuming a standard continental aerosol size distribution and a subarctic summer atmospheric profile. It was found that neglecting the atmospheric effect may lead to an error of 0.5 K. As this error is rather small and because it is constant over the entire area it was disregarded. It has to be noted that we are mainly interested in the relative temperature distribution, not in the absolute one.

Ground-based in-situ temperature measurements on three different roof locations agree with the temperatures derived from the airborne sensor data within -0.7 K and -4.7 K. Fig. 2 shows the positions where the temperatures were compared; the measurements are shown in Tab. 1. Note that no emissivity was taken into account and the differences in Tab. 1 are mostly due to emissivity of the material and the minor atmospheric effect. The measurements were carried out during the overpass of the aircraft. In addition, continuous air temperature data were recorded. These data show the current air temperature (between 6 °C and 7 °C) from 3 am to 7 am Central European Summer Time. The flight mission took place between about 6 am and 7 am.

3.3 *AISA+*

The processing of the hyperspectral data includes the boresight calibration, radiometric
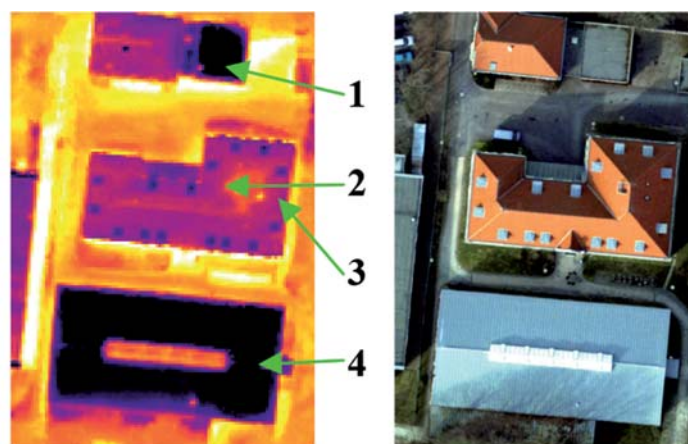

Fig. 2: In-situ temperature measurement points, thermal image on the left side, RGB ortho image on the right. The numbers indicate the measurement points.

Tab. 1: Temperatures at the in-situ measurement points (Fig. 2).

Position	Thermal image (K)	In-situ measurement (K)	Delta (K)
1	275.7	276.5	-0.8
2	278.7	282.1	-3.4
3	279.4	284.1	-4.7
4	275.8	276.5	-0.7

correction, rectification, georeferencing, orthorectification, and mosaicking.

Due to partial cloudy weather conditions it was decided to use the FODIS ratio (Homolova et al. 2009) to represent the reflectance rather than the reflectance derived from the atmospheric correction model. The FODIS ratio is the ratio of the down welling irradiance, measured by the FODIS detector, which is part of the AISA system and mounted on top of the aircraft, and upwelling radiance, measured by the AISA sensor without any atmospheric correction.

Under partial cloudiness the FODIS ratio provides better results than the reflectance derived from an atmospheric correction model, which is based on a radiative transfer model. This is due to the fact that atmospheric correction algorithms always assume clear skies with no clouds. In the case of the AISA+ system operated below clouds, the reflected radiation as well as the downwelling radiation drops rapidly. However, the FODIS ratio will stay almost as constant when having the same surface characteristics. Applying an atmospheric correction model for the reflectance calculation would result in unrealistically small reflectance values.

In order to achieve a high geometric accuracy, the hyperspectral sensor AISA was calibrated using a new procedure developed by the project group (Piechel et al. 2011). It turned out that the results from this calibration cannot be used in the CaliGeo (SPECIM 2010) tool, which is the default processing software delivered with the sensor system. Despite of the fact that the documentation describes the possibility to use a factor for radial distortion, it turned out that the software is not able to calculate useful results when using this factor. The lens distortion error is about 4 pixels

for the outermost pixel of the sensor and still remains in the georeferenced image. Fig. 3 shows the pre-processed FODIS ratio CIR colour image generated from the AISA+ data. Some dark and bright spots within the image are caused by the cloudiness.

To verify the spectral measured data, in-situ measurements with a field spectrometer were carried out. The reflectance of different roof tops was collected using a RAMSES VIS SAM-8103 field spectrometer. Some example reflectance curves and FODIS ratio curves are shown in Fig. 4. It has to be noted that the portable spectrometer measurements only had non-calibrated white Teflon as a white reference, and that some of the measurements were taken at a time different from the time the imagery was acquired. Taking into account the diversities of the instrumentation of the measuring setups and of the illumination, a comparison by visual examination indicates a sufficiently good agreement between airborne and reference spectra.

Direct georeferencing of the hyperspectral data resulted in discrepancies between 0.0 m and 2.0 m. At this time, the reasons for the larger discrepancies are subject to speculation. It is likely that residual boresight errors

Fig. 3: A 500 m × 500 m subset of the pre-processed CIR reflectance image generated from three AISA+ strips. The spatial resolution is 50 cm. Note the sunny part of the lower strip compared to the other strips.
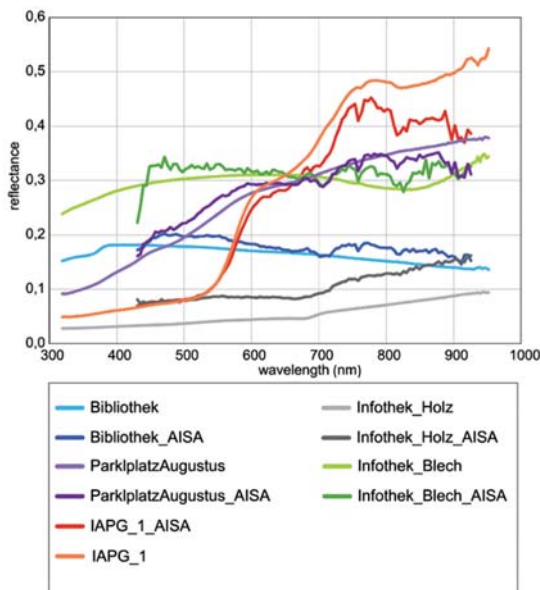
Fig. 4: AISA FODIS ratios (dark) and portable spectrometer reflectance (bright colours). The names indicate the places where the field spectrometer measurements took place.

or time drifts of the AISA+ system may cause the disagreement. In order to compensate these errors the hyperspectral data were co-registered to the RGB ortho-mosaic and rectified by a fourth-degree polynomial rubber-sheeting using hundreds of manually picked control points. The rectified image with a GSD of 50 cm was used as a basis for generating an image corresponding to the normalised difference vegetation index (NDVI), which was one of the inputs for building classification (section 4).

3.4 Airborne Laser Scanner LMS Q560

For airborne laser scanning the positions and orientations are based on GNSS/INS measurements. The accuracy of the airborne laser scanning data strongly depends on an accurate processing of the GNSS/INS data. In order to achieve the highest possible internal precision of the laser data in position and height a number of requirements have to be considered:

a) Accurate determination of the calibration values, i.e. installation offset parameters and boresight angles between scanner and IMU, if possible for each flight session.

b) Use of exact lever arms between GNSS antenna and IMU as well as between IMU and laser scanner.

c) Precise internal calibration of the instrument.

The LMS Q560 allows for collecting full waveform laser data. For the current project only the first/last pulses are needed. The Riegl software enables to extract the first/last pulse data from the full waveform data (Petrie 2011). To derive digital elevation models from airborne laser data a number of processing steps are necessary. At first morphological filtering is carried out automatically using the software package TerraScan (TERRASOLID 2010). The results were visually verified and a locally optimized filter parameter is applied in an iterative process to improve the results. As final products a digital surface model (DSM) and a digital terrain model (DTM) are generated as raster models with a grid width of 25 cm. Homogeneous regions are easier to be classified than city centres. The accuracy also depends on the laser point density, which is about 23 points/m^2 in our test. From the DSM and the DTM, products such as contour lines and cross sections can be inferred.

In addition to the DSM and the DTM, the original point cloud is also available. Fig. 5 shows a shaded relief of the DSM.
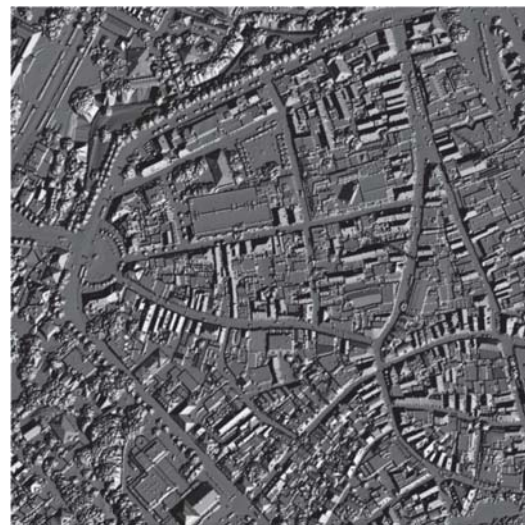

Fig. 5: A shaded relief of a 500 m × 500 m subset of the DSM.

4 Products and Analysis

After pre-processing, various products are derived in the ways described in the subsequent sections.

4.1 *Temperature Distribution within Buildings*

In most cases, the relative differences of the roof temperatures are sufficient to indicate heat bridges or heat losses.

As we were only interested in the temperature distribution on buildings, we first detected buildings by a simple decision tree algorithm. For that purpose, we used the NDVI generated from the hyperspectral data and a normalized DSM (nDSM). The nDSM was calculated by subtracting the DTM from the DSM (nDSM = DSM – DTM). Pixels were considered to correspond to building pixels if the NDVI is smaller than 0.35 and if the nDSM height is greater than 7 m. These thresholds were found empirically. The non-building pixels correspond to the black areas in Fig. 6.

Finally, we visualised the temperature distribution inside the areas detected as buildings using a lookup table with a colour scale with steps of 1 K (Fig. 6). Thus, the potential heat loss can be visualized far more efficiently than with a continuous presentation. One can see that the temperature is not evenly distributed over the buildings. This is caused by emissivity changes of different roof materials or by heat bridges. Generally one speaks of a heat bridge if the temperature differences within an object of constant emissivity are more than 5 K. Fig. 6 shows the temperature distribution within the selected area.

4.2 *Solar Potential*

To assess the solar potential it is important to know the alignment of roofs within a city. In order to estimate the potential of solar energy in general the number of flat roofs and roofs with a certain inclination and orientation as well as the total area of such roofs has to be known.
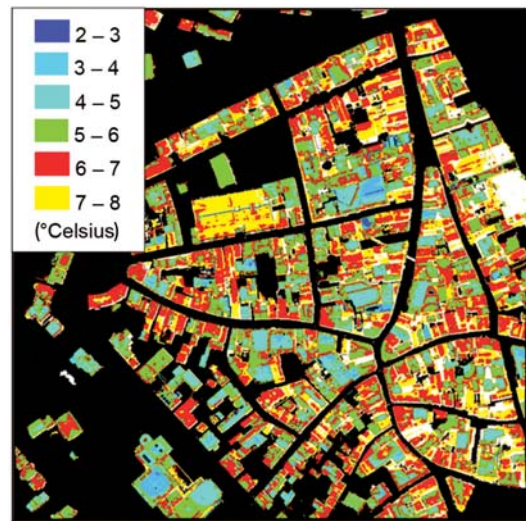

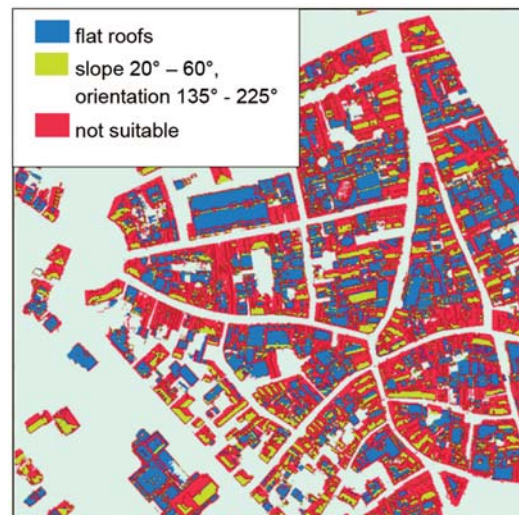**Fig. 6:** Building temperature distribution in a 500 m × 500 m subset of our test site.

Fig. 7: Potential for the use of solar panels of Oldenburg, 500 m × 500 m subset.

If an offset of ± 10 % from the optimal alignment is acceptable then inclinations of 20° to 60° with an azimuth between 135° and 225° (DGS 2012) can be regarded as favourable. These data are valid for Germany and vary slightly depending on the local climate.

The roof orientations were derived from nDSM data. The computations were based on the building mask derived as described in section 4.1. The slopes are computed for all pixels marked as "building" in this mask. The computation is based on a local quadratic surface

fitting of the DSM, taking into account 3 × 3 pixels. Again, a decision tree was used to decide whether a pixel is in an area favourable for solar panels. If the slope was less than 10°, the pixel was regarded as being on a flat roof, and therefore marked in blue. If the slope was between 20° and 60° and the orientation of the roof was between 135° and 225°, the pixel was marked in green. This indicates that it is in an area with favourable conditions for installing solar panels. The pixels marked in red indicate areas that are not suitable. The results of the decision tree classification are presented in Fig. 7. In the inner city only a small number of houses, shown in green, is ideal for installing solar panels. Additionally, buildings with flat roofs, marked in blue, are suitable for panels mounted on stilts.

4.3 Building Classification

The roof classification aims to separate different roof surface materials. The classification consists of two parts. One part is the binary classification of the roofs. The other part is a classification of the surface material of these roofs.

The first step, the roof classification, is based on the rasterized ALS data, the NDVI calculated from the hyperspectral data and the plane normals calculated from the original point cloud. The plane normal is calculated using the robust least median of squares technique for plane fitting using all ALS points within 1×1 m^2 cells. These raster cells are resampled to 50 cm to match the other data.
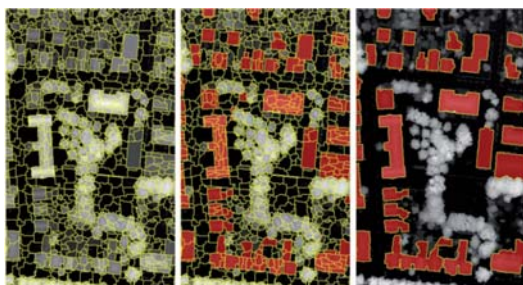

Fig. 8: From left to right: raw segmentation (yellow = segment boundary), initial classification (roofs = red), classification after rule set and merging; the background is the nDSM image.

The nDSM and three raster images representing the components of the normals are used for a segmentation using eCognition's multiresolution segmentation (BAATZ & SCHÄPE 2000). The parameters of the segmentation algorithm were set to achieve an oversegmentation in order to make sure that all the building boundaries are represented by segment boundaries. A larger segment size (higher scale parameter in eCognition) results in a higher risk to miss a building boundary. The left image of Fig. 8 shows the initial segmentation.

Then, the roof segments were classified via thresholds, using the nDSM height (higher than 2.5 m) and NDVI (less than 0.42) as shown in the centre part of Fig. 8. The threshold values used here are different from the ones used before because we are now working on the basis of segments and not on the basis of pixels.

The classification was followed by some refinements using a set of rules for the image segments, e.g. to delete small objects and remove objects with a shape not typical for buildings, e.g. very thin objects with a high percentage of borders to non-roof objects. The resulting building mask is shown in the right part of Fig. 8.

For accuracy assessment, all roofs in an area of 900 m × 300 m were digitized manually from the RGB true orthophoto generated on the basis of a DSM from image matching (section 3.1). The total roof area used for a man-

Tab. 2: Classification accuracy of the binary roof classification.

Ground truth classification	Background (%)	Roof (%)
Background	96.29	8.03
Roof	3.71	91.97

Tab. 3: Producer's and user's accuracy of the binary roof classification.

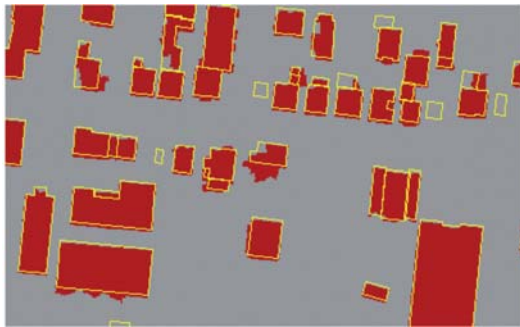| Ground truth classification	Producer's accuracy (%)	User's accuracy (%)
Background	96.29	97.63
Roof	91.97	87.83

Fig. 9: Classified roofs (red) and digitized building outlines (yellow).

ual accuracy assessment is about 74,000 m². About 92 % of all roof pixels were found correctly (for details, see Tabs. 2 and 3). The overall accuracy is 95.3 % and the kappa coefficient is 0.87. Errors result from some completely missed roofs, e.g. low garage-like buildings with heights near the nDSM threshold (2.5 m) and some roofs that are partly hidden by trees. Fig. 9 shows an example area with typical errors. It can be seen that some small buildings and building parts are missing. Errors in the reference also contribute to the overall error budget, but these errors are much lower than the actual classification errors.

4.4 *Roof Material Classification*

For the roof material classification a pixel-based and a segmentation-based approach were combined.

Reference data were generated by visual classification based on the true orthophoto mosaic, the manually digitized roof outlines used as a reference for the evaluation in sec-

tion 4.3 (yellow lines in Fig. 9) and terrestrial photographs of roofs. Only roofs with mostly homogenous material were considered to be suitable as a reference. Thus, we selected as a reference only roofs consisting of only one material and a few (< 15 % in area) disturbing objects like dormers and chimneys as a reference. Within each reference roof, 4 to 20 pixels were manually selected as training pixels so that they completely correspond to the main roof material, to ensure that training pixels represent the correct material.

To reduce the training data and speed up the computation, only a subset of pixels was randomly selected as the final training pixels. Tab. 4 shows the amount of training data selected and used for classification.

In the literature SVM-based classification proved to be very suitable for classifying hyperspectral data (Melgani & Bruzzone 2004, Plaza et al. 2009, Waske et al. 2009, Braun et al. 2012). The reduced training subset was, thus, used to train a SVM for classification, using the software by Rabe et al. (2009). A radial basis function (RBF) kernel with the parameter $g = 1$ was used. Both g and soft margin parameter $C (= 100)$ were determined by a 3 fold cross validation. The SVM is applied to classify each pixel independently.

To define a single material per roof, a majority voting is used to transfer the pixel-based classification results to the roof objects. That is, the material of each roof is determined as the material of the majority of all pixels inside that roof. The parts of Fig. 10 show an example with the results from the SVM classification and the final majority voting.

The confusion matrix in Tab. 5 shows the outcome of the classification and Tab. 6 shows the user's and producer's accuracies. The re-

Tab. 4: Training area size and subset size.

Material	Manually selected training pixels	Final training subset
Red roofing tiles	568	200
Black roofing tiles	648	200
Brown roofing tiles	18	18
Metal	62	50
Tar paper	271	150
White colour	31	31

metal   black roofing tiles   brown roofing tiles
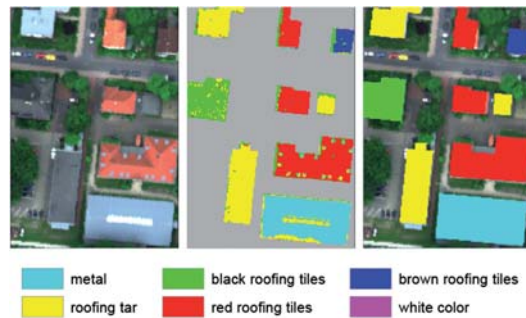
roofing tar   red roofing tiles   white color

Fig. 10: Roof material classification. Left: RGB image (from hyperspectral data), centre: SVM classification with background masked in grey, right: results of material classification after majority voting.

sults for all materials except brown roofing tiles are very promising. The poor results for brown roofing tiles have to be analysed with care because of the very low sample size and seem to be caused by a high spectral overlap with the black and red roofing tiles.

The SVM classification works well when using a sufficient number of training data. The training data need to cover all possible characteristics of a roof material. In this way, one can be certain to get the best support vectors for defining the class boundaries. Additionally, it can be confirmed that the SVM classification works quite well with noisy data. The mean signal-to-noise ratio of the hyperspectral data was only about 100, averaged over all spectral channels and all spatial pixels.

Tab. 6: Producer's and user's accuracies of the roof material classification.

	Producer's accuracy (%)	User's accuracy (%)
Red roofing tiles	97.1	98.6
Black roofing tiles	97.8	93.5
Brown roofing tiles	50.0	100.0
Roofing tar	89.3	96.2
White colour	100.0	100.0
Metal	100.0	100.0

5 Conclusions and Outlook

From different kinds of remote sensing data, products such as temperature distributions of roof tops and maps of the suitability of roofs for installing solar panels were derived by first detecting buildings based on a simple decision tree and further analysis steps. From hyperspectral data the roof material characteristics are inferred using a SVM-based classification. The fusion of different datasets makes it possible to obtain more information by synergic use of the derived products. It is important to note that a precise georeference of all data is the basis for reliable results.

Regarding the roof and material classification, additional refinements could be done using the slope per roof plane as an additional feature. This may help because roofing tiles are only used on sloped roofs.

Tab. 5: Confusion matrix of the roof material classification. The numbers correspond to the number of roof polygons, not to pixels.

Ground truth classification	Red	Black	Brown	Tar	White	Metal	Total
Red roofing tiles	67	1	0	0	0	0	68
Black roofing tiles	2	87	1	3	0	0	93
Brown roofing tiles	0	0	1	0	0	0	1
Roofing tar	0	1	0	25	0	0	26
White colour	0	0	0	0	1	0	1
Metal	0	0	0	0	0	5	5
Total	69	89	2	28	1	5	194

Some georeferencing errors remaining in the hyperspectral data lead to misclassifications at the building boundaries. In addition, some misclassifications are induced by different solar illumination angles depending on the roof alignment and on the recording time. The reduction of these errors is a part of the ongoing research.

A further goal is to combine the complete roof mask with the SVM classification to obtain the material per roof for the whole area.

Acknowledgements

References

Baatz, M. & Schäpe, A., 2000: Multiresolution segmentation – an optimization approach for high quality multi-scale image segmentation. – Strobl, J., Blaschke, T. & Griesebner, G. (eds): Angewandte Geographische Informations-Verarbeitung **XII:** 12–23, Wichmann Verlag, Karlsruhe.

Bähr, H.-P., Lemp, D. & Weidner, U., 2005: Hyperspectral meets Laserscanning: Image Analysis of Roof Surfaces. – ISPRS Hannover Workshop, High-Resolution Earth Imaging for Geospatial Information.

Bannehr, L., Hannusch, D., Jany, S. & Runne, H., 2006: Komplexes modulares System zur Ableitung von Umweltparametern. – Seyfert, E. (Hrsg.): **26.** Wissenschaftlich-Technische Jahrestagung der DGPF: 295–302.

Berk, A., Anderson, G.P., Acharya, P.K., Bernstein, L.S., Muratov, L., Lee, J., Fox, M., Adler-Golden, S.M., Chetwynd, J.H., Hoke, M.L., Lockwood, R.B., Gardner, J.A., Cooley, T.W., Borel, C.C., Lewis, P.E. & Shettle, E.P., 2006: MODTRAN5: 2006 Update. – SPIE **6233** (62331F).

Braun, A.C., Weidner, U., Jutzi, B. & Hinz, S., 2012: Kernel Composition with the one-against-one Cascade for Integrating External Knowledge into SVM Classification. – PFG – Photogrammetrie, Fernerkundung, Geoinformation **2012** (4): 371–384.

DGS, 2012: Leitfaden Solarthermische Anlagen. – 9. Auflage 2012, Deutsche Gesellschaft für Sonnenenergie (Hrsg.), ISBN 978-3-9805738-0-1.

Homolova, L., Alanko-Huotari, K. & Schaepman, M.E, 2009: Sensitivity of the ground-based downwelling irradiance recorded by the FODIS sensor in respect of different angular positions. – First IEEE GRSS Workshop on Hyperspectral Image and Signal Processing: Evolution in Remote Sensing (WHISPERS), Grenoble, France.

Heldens, W., Heiden, U., Esch, Th. & Dech, S., 2010: Potential of Hyperspectral Data for Urban Micro Climate Analysis. – Hyperspectral Workshop 2010, Frascati, Italy.

Hilling, F. & de Lange, N., 2010: Webgestützte interaktive Solardachkataster. Ein Instrument zur Darstellung der Nutzungseignung von Dächern für Photovoltaikanlagen am Beispiel der Stadt Lage. – Standort **34** (4): 104–109.

Hirschmüller, H., 2008: Stereo Processing by Semiglobal Matching and Mutual Information. – IEEE Transactions on Pattern Analysis and Machine Intelligence **30** (2): 328–341.

Klärle, M., Ludwig, D. & Lanig, S., 2009: SUN-AREA – Ein Beitrag der Fernerkundung gegen den Klimawandel. – ZfV **2009** (2): 71–78.

Kokkas, N. & Dowman, I.J., 2006: Fusion of Airborne Optical and LIDAR Data for Automated Building Reconstruction. – ASPRS Annual Conference, Reno, USA.

Lemp, D. & Weidner, U., 2004: Use of Hyperspectral and Laser Scanning Data for the Characterization of Surfaces in Urban Areas. – **XXth** ISPRS Congress, Commission VII.

Lemp, D. & Weidner, U, 2005: Improvements of Roof Surface Classifications Using Hyperspectral and Laser Scanning Data. – IAPRSIS **XXX-VI-8/W27**, ISPRS Joint Conferences, Tempe, USA.

Luhmann, T., Ohm, J., Piechel, J. & Roelfs, T., 2011: Geometrische Kalibrierung von Thermografiekameras. – PFG – Photogrammetrie, Fernerkundung, Geoinformation **2011** (1): 5–15.

Melgani, F. & Bruzzone, L., 2004: Classification of Hyperspectral Remote Sensing Images with Support Vector Machines. – IEEE Transactions on Geoscience and Remote Sensing **42:** 1778–1790.

Mori, M., Iwata, T., Minami, Y., Kato, S. & Akamatsu, Y., 2008: Spectral Analysis of Building Materials Used in Japan. – International Archives of the Photogrammetry, Remote Sensing and Spatial Information Sciences **XXXVII** (B8), Beijing, China.

Petrie, G., 2011: Airborne Topographic Laser Scanners. – GeoInformatics **1:** 34–44.

Piechel, J., Bannehr, L., Luhmann, T., Roelfs, T. & Schmidt, A., 2011: Geometrische Kalibrierung von Hyperspektralsensoren. – DGPF-Jahrestagung, Mainz.

Plaza, A., Benediktsson, J., Boardman, J., Brazile, J., Bruzzone, L., Camps-Valls, G., Chanussot, J., Fauvel, M., Gamba, P., Gualtieri, A., Marconcini, M., Tilton, J.C. & Trianni, T., 2009: Recent Advances in Techniques for Hyperspectral Image Processing. – Remote Sensing of Environment **113:** 110–122, Elsevier.

Quinlan, J.R., 1986: Induction of decision trees. – Readings in Machine Learning **1** (1): 81–106.

Rabe, A., van der Linden, S. & Hostert, P., 2009: imageSVM, Version 2.0, software available at www.hu-geomatics.de (18.3.2013).

Rentsch, M. & Krzystek, P., 2009: Lidar Strip Adjustment Using Automatically Reconstructed Roof Shapes. – ISPRS Workshop High-Resolution Earth Imaging for Geospatial Information, Hannover.

Roessner, S., Segl, K., Heiden, U. & Kaufmann, H., 2001: Automated Differentiation of Urban Surfaces Based on Airborne Hyperspectral Imagery. – IEEE Transaction on Geosciences and Remote Sensing **39:** 1525–1532.

Rottensteiner, F., Sohn, G., Jung, J., Gerke, M., Baillard, C., Benitez, S. & Breitkopf, U., 2012: The ISPRS Benchmark on Urban Object Classification and 3D Building Reconstruction. – ISPRS Annals of the Photogrammetry, Remote Sensing and Spatial Information Sciences **I** (3), XXII ISPRS Congress Melbourne.

SPECIM, 2010: CaliGeo 4.9.9 AISA Data Processing Tool. – Operating Manual. Spectral Imaging Ltd., Oulu, Finland.

Steinwart, I. & Christmann, A., 2008: Support Vector Machines. – 602 p., Springer, New York.

TERRASOLID, 2010: TerraScan User's Guide. – Arttu Soininen, Finland.

Waske, B., Benediktsson, J., Árnason, K. & Sveinsson, J., 2009: Mapping of Hyperspectral AVIRIS Data Using Machine-learning Algorithms. – Canadian Journal of Remote Sensing **35:** 106–116.

Yang, X. (ed.), 2011: Urban Remote Sensing: Monitoring, Synthesis and Modelling in the Urban Environment. – 408 p., Wiley-Blackwell.

Addresses of the Authors:

Lutz Bannehr & Andreas Schmidt, Hochschule Anhalt, Institut für Geoinformation und Vermessung, Bauhausstraße 8, D-06846 Dessau-Roßlau, Tel.: +49-340-5197-1551, e-mail: {l.bannehr}{and.schmidt}@afg.hs-anhalt.de

Thomas Luhmann & Johannes Piechel, Jade Hochschule Oldenburg, Institut für Angewandte Photogrammetrie und Geoinformatik, Ofener Straße 16, D-26121 Oldenburg, Tel.: +49 441-7708-3172, e-mail: {thomas.luhmann}{johannes.piechel}@jade-hs.de